

Electron Energization by Turbulent Electric Fields: A Possible Source of the Outer Radiation Belt

Maria E. Usanova¹ and Robert E. Ergun¹

¹University of Colorado Boulder

November 22, 2022

Abstract

The turbulent energy cascade that is characteristic of bursty bulk flow (BBF) braking regions in the Earth's magnetotail has been shown to be the energy source for large-amplitude electric fields (>50 mV/m) which can, in turn, result in local energetic electron acceleration. These pre-energized electrons move inward to stronger magnetic fields being adiabatically energized and can eventually supply an energetic tail to electron distributions in the outer radiation belt. Using wave and plasma measurements from the Time History of Events and Macroscale Interactions during Substorms (THEMIS) satellites during four tail seasons from 2015 to 2019, we study the process of BBF magnetic and kinetic energy being transferred to electrons by turbulent electric fields from a statistical perspective. We identify turbulent BBF regions by the presence of high-amplitude electric fields. We show that the high-amplitude electric fields are associated with an increase in electron temperature by three times compared to quiet times and with a ten-fold increase in temperature fluctuations. They are also associated with strong variations of energetic electron fluxes, indicative of local acceleration. We further discuss the implications of these findings and the role of this pre-energized electron population in supplying the outer radiation belt.

1 **Electron Energization by Turbulent Electric Fields: A Possible Source of the Outer**
2 **Radiation Belt**

3

4 ¹M.E. Usanova and ^{1,2}R.E. Ergun

5

6 ¹Laboratory for Atmospheric and Space Physics, University of Colorado, Boulder,
7 Colorado, USA

8 ²Department of Astrophysical and Planetary Sciences, University of Colorado, Boulder,
9 Colorado, USA

10

11 **Abstract**

12 The turbulent energy cascade that is characteristic of bursty bulk flow (BBF) braking
13 regions in the Earth's magnetotail has been shown to be the energy source for large-
14 amplitude electric fields (>50 mV/m) which can, in turn, result in local energetic electron
15 acceleration. These pre-energized electrons move inward to stronger magnetic fields
16 being adiabatically energized and can eventually supply an energetic tail to electron
17 distributions in the outer radiation belt. Using wave and plasma measurements from the
18 Time History of Events and Macroscale Interactions during Substorms (THEMIS)
19 satellites during four tail seasons from 2015 to 2019, we study the process of BBF
20 magnetic and kinetic energy being transferred to electrons by turbulent electric fields from
21 a statistical perspective. We identify turbulent BBF regions by the presence of high-
22 amplitude electric fields. We show that the high-amplitude electric fields are associated
23 with an increase in electron temperature by three times compared to quiet times and with
24 a ten-fold increase in temperature fluctuations. They are also associated with strong
25 variations of energetic electron fluxes, indicative of local acceleration. We further discuss
26 the implications of these findings and the role of this pre-energized electron population in
27 supplying the outer radiation belt.

28

29 **Main point #1.** Large-amplitude electric fields are associated with ten-fold electron
30 temperature fluctuations and energetic electron flux variations.

31 **Main point #2.** Temperature and flux variations rather than absolute temperature and flux
32 values are indicative of local acceleration.

33 **Main point #3.** The accelerated electrons may serve as a seed population for the high-
34 energy tail of the outer radiation belt.

35

36 **1. Introduction**

37 Bursty bulk flows (BBFs) are high-speed plasma flow events, observed in Earth's plasma
38 sheet (Baumjohann et al., 1990; Angelopoulos et al., 1992). They are believed to be
39 generated by magnetic reconnection in the tail at distances greater than about ~20-30
40 Earth radii (R_E) (Chen and Wolf, 1993). Earthward BBFs observed in the plasma sheet
41 within a wide range of geocentric distances from 5 to 30 R_E are characterized by
42 dipolarization (an increase in the B_z magnetic field component) and a decrease in plasma
43 density and plasma pressure (Ohtani et al., 2004). BBFs are spatially localized in the
44 direction of the flow and are often confined to $<3 R_E$ in the dawn-dusk direction
45 (Angelopoulos et al., 1997). Due to their localization, these events are most often
46 observed as bursts ~10 min duration. Between 10 and 20 R_E their speeds reach several
47 hundred to over a thousand km/s in earthward direction. As BBFs move closer to Earth
48 (6-12 R_E tailward), they slow down and deflect as their energy dissipates (Shiokawa et
49 al., 1997). The region over which the flow is slowed and diverted in the near-Earth tail is
50 known as the BBF braking region.

51 The flow braking can generate turbulent plasma fluctuations and instabilities (e.g.,
52 Shiokawa et al., 2005; El-Alaoui et al., 2013). These fluctuations can exhibit properties of
53 MHD- and kinetic scale Alfvén waves being involved in a turbulent cascade in BBFs
54 (Chaston et al., 2012, 2014; Stawarz et al., 2015). The energy cascade has also been
55 found associated with tail reconnection (Dai et al., 2011; Ergun et al., 2020) and observed
56 in the plasma sheet boundary layer between 4 and 6 R_E (Wygant et al., 2002).

57 Ergun et al. (2015) found that BBF braking events can be accompanied by high-amplitude
58 electric fields (>50 mV/m). The large-amplitude electric fields have been observed at
59 radial distances between 10 and 13 R_E (Sigsbee et al., 2002) and as far in as
60 6 R_E (Nishimura et al. 2008; Chaston et al., 2014), consistent with the BBF braking

61 location. These large-amplitude electric field events share a number of characteristics
62 such as enhanced magnetic field fluctuations, magnetic field dipolarization, fluctuating ion
63 flow velocities, ion and electron heating, and strong, field-aligned Poynting flux which
64 might be responsible for the generation of Alfvénic aurora (Dubyaagin et
65 al., 2010; Nakamura et al., 2014). A significant portion of electric field spectral power
66 density typical to these events is above the ion cyclotron frequency. It often contains
67 nonlinear Debye scale structures, also known as time domain structures, i.e., double
68 layers and electron phase space holes (Ergun et al., 2009; 2015). The spectra of low-
69 frequency electric and magnetic field fluctuations also found to exhibit power law behavior
70 that may be indicative of turbulence. Stawarz et al. (2015) hypothesized that Alfvénic
71 turbulence is generated in the BBF braking region at the expense of the free energy in
72 the BBF. Small-scale Alfvén waves (e.g., Lysak et al., 2009) or Alfvénic turbulence (e.g.,
73 Karimabadi et al., 2013) can drive strong, localized, currents and electron beams which
74 may provide the source for the observed large-amplitude electric fields (Kindel and
75 Kennel, 1971; Newman et al., 2001; Ergun et al., 2005). In addition, strong turbulence
76 may produce the necessary conditions for the development of a significant nonthermal
77 tail in both the electron and ion distributions (Ergun et al., 2020). The turbulence cascades
78 the driving energy to smaller scales and higher frequencies at which electrons can
79 efficiently absorb energy. Turbulence also generates magnetic depletions that trap the
80 particles and impart unequal dwell times, causing relatively few particles to absorb a
81 disproportionately large amount of energy.

82 BBFs contribute a large fraction of the observed mass, energy, and magnetic flux
83 transport towards Earth in the magnetotail (Baumjohann et al., 1990; Angelopoulos et
84 al., 1994). Even though these flows are sporadic, they can have a significant impact on
85 the energetic particle dynamics in the magnetosphere. Transient dipolarizations within
86 BBFs (also known as dipolarization fronts) are often accompanied by dispersionless
87 particle injections - simultaneous sudden particle flux enhancements at energies of tens
88 to hundreds keV (e.g., Gabrielse et al., 2012; 2014; Liu et al., 2016) - indicative of local
89 acceleration process. Injections play an important role in the inner magnetosphere
90 dynamics by providing a source population (10 - 300 keV ions and electrons) for the ring

91 current and outer radiation belt. Deep injections can supply even higher energy electrons,
92 up to a few MeV as observed inside geosynchronous orbit by Dai et al. (2015).

93 The relative importance of large-scale electric and magnetic fields in the acceleration and
94 transport of injected particles is still debatable. Numerically, this problem is usually
95 studied by test-particle simulations of electron and ion trajectories in the dipolarization
96 electric and magnetic fields in the magnetotail. Originally, the energization was suggested
97 to be associated with ExB drift in the inductive electric field due to betatron (conserving
98 the first adiabatic invariant) and Fermi acceleration (conserving the second adiabatic
99 invariant) or a combination thereof (e.g., Williams et al., 1990). Later, non-adiabatic
100 effects have become the focus of attention. For example, Delcourt (2002) demonstrated
101 that the nonadiabatic ion behavior can lead to significant local acceleration, mainly in the
102 direction perpendicular to the background magnetic field. Since particles with larger
103 Larmor radii are unmagnetized more easily, they are much more susceptible to
104 energization by a local electric field.

105 Recent test particle simulations in high-resolution MHD fields have shown that
106 depolarization fronts can provide conditions for magnetic trapping and further particle
107 energization even in the absence of large electric fields (Ukhorskiy et al., 2017, 2018;
108 Sorathia et al., 2018). However due to their intrinsic global nature, the MHD models are
109 not suitable to simulate local wave-particle interactions and have a limiting factor in
110 accurately reproducing the highest-energy outer belt electron fluxes. Therefore, to model
111 kinetic effects and study their role in the dynamics of the magnetotail three-dimensional
112 global kinetic simulations are warranted.

113 In this paper, we expand on the Ergun et al. (2015) study and investigate the relationship
114 between the observed turbulent electric fields and electron energization in BBFs. In
115 Section 2, we describe THEMIS orbits and instrumentation used for this study. In Section
116 3, we present an event example showing the relationship between the strong electric
117 fields and electron heating. In Section 4, we describe the automated event detection
118 algorithm and BBF selection criteria. In Section 5, we examine the relationship between
119 the electric field amplitudes and electron temperature and energetic flux fluctuations. In

120 Section 6, we discuss the role of pre-energized electron population in supplying the outer
121 radiation belt. Section 7 concludes our study.

122 **2. Instrumentation**

123 The Time History of Events and Macroscale Interactions during Substorms (THEMIS) is
124 a mission originally employing five identical spacecraft launched on February 17, 2007
125 (Angelopoulos, 2008). In December 2009, THEMIS B and C were sent to the Moon, while
126 the remaining three probes continued orbiting the Earth at ~ 10 -15 Re apogee, THEMIS
127 D being on the highest elliptical orbit. The probes carry instrumentation to measure
128 electric and magnetic fields as well as charged particles at several time resolutions. For
129 this study, we use data from Electric Field Instrument (EFI) (Bonnell et al., 2008; Cully et
130 al., 2008), Fluxgate Magnetometer (FGM) (Auster et al., 2008), electrostatic analyzer
131 (ESA) electron measurements in the a few eV up to 30 keV energy range (McFadden et
132 al., 2008), and Solid State Telescopes (SST) electron differential energy flux within the
133 energy range from 41 to 203.5 keV (Angelopoulos et al., 2008). We surveyed a total of
134 1038 days of data from probes A, D and E during the tail seasons of 2015-2019.

135

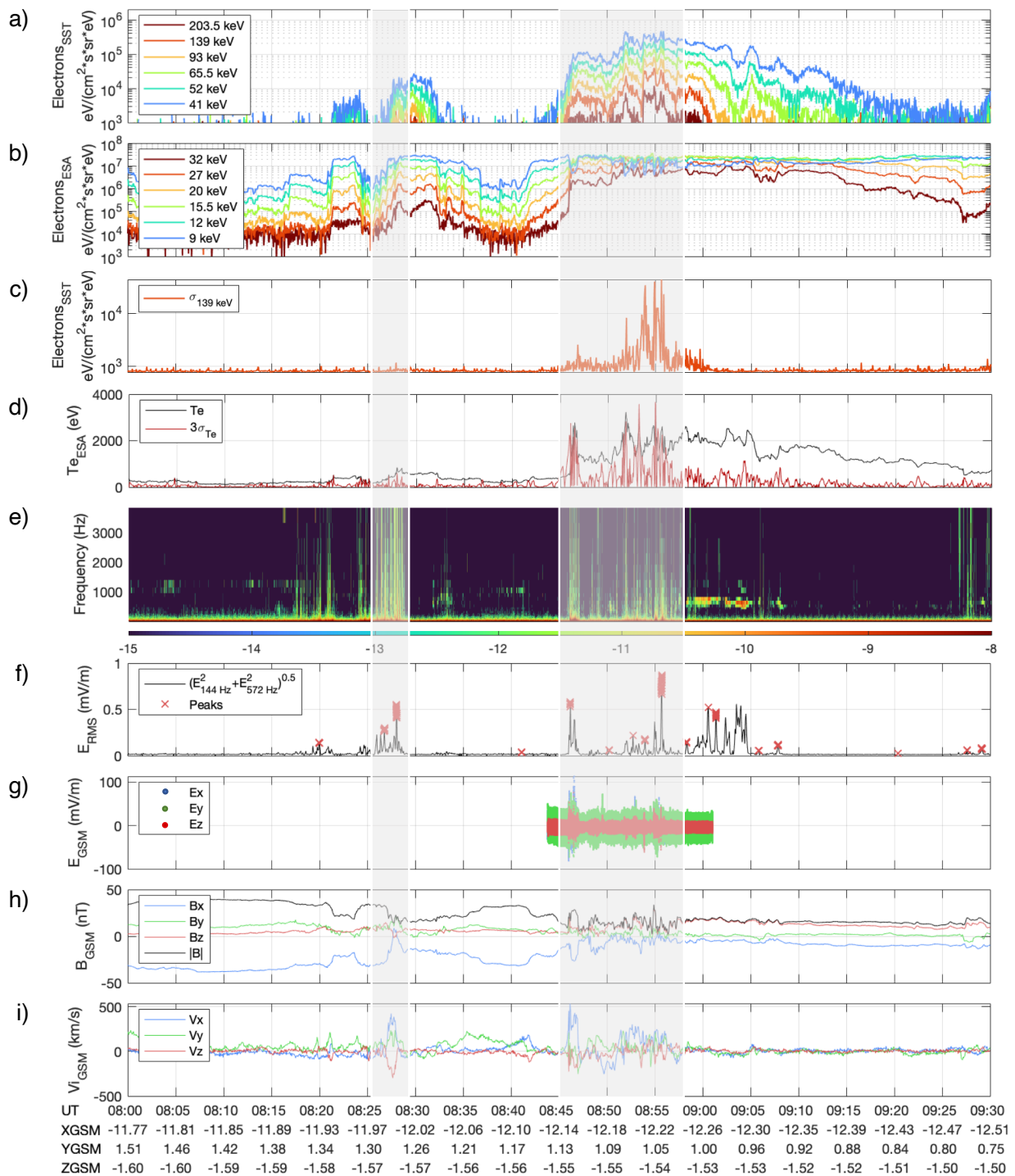
136 **3. Observations**

137 An example of event of interest is shown in Figure 1. The event was observed on THEMIS
138 A at 08:26-08:28 and 08:45-08:57 UT on March 5, 2018. Panel a) shows enhancements
139 in the SST omnidirectional electron differential energy flux from six energy channels
140 spanning 41 to 203.5 keV. These enhancements are also seen in the ESA omnidirectional
141 electron differential energy flux from six energy channels between 9 and 32 keV in Panel
142 b). In addition, SST flux variations and ESA temperature fluctuations were calculated by
143 removing a continuous, linear trend over a 100 s interval. SST electron differential energy
144 flux variations in the 139 keV channel are shown in Panel c). ESA electron temperature
145 (black) and temperature fluctuations (red) are plotted in Panel d). Panels e) and f) show
146 an on-board computed electric field spectrogram and filterbank (FBK) electric field root
147 mean square (RMS) amplitude of the 144 and 572 Hz frequency bins, respectively.
148 Electric field peaks selected with an automated algorithm (discussed in section below)
149 applied to the FBK data are shown by the red crosses. Electric field components in burst

150 mode, B_x , B_y , B_z , and $|B|$ magnetic field, and ion V_x , V_y , V_z velocity components are
151 shown in Panels g), h) and i). The electric and magnetic time series and ion velocities are
152 plotted in GSM coordinates.

153 Overall, the events are characterized by the presence of strong, up to ~ 100 mV/m, electric
154 fields, fluctuations in magnetic field and ion velocity, and electron heating and
155 acceleration. The intervals where they are observed are shaded by the grey bars.

156 Remarkably, the strong electric fields are well correlated with variations in electron fluxes
157 over a wide range of energy, covering both ESA and SST measurements. We argue that
158 these variations indicate a local acceleration process.



159

160 **Figure 1.** Summary plot of an event example from THEMIS A at 08:26-08:28 and 08:45-
 161 08:57 UT on March 5, 2018. a) SST omnidirectional electron differential energy flux in the
 162 41, 52, 65.5, 93, 139 and 203.5 keV energy channels; b) ESA omnidirectional electron
 163 differential energy flux in the 9, 12, 15.5, 20, 27 and 32 keV energy channels; c) SST

164 electron differential energy flux variations in the 139 keV energy channel; d) ESA electron
165 temperature (black) and temperature fluctuations (red); e) electric field spectrogram; f)
166 on-board computed FBK electric field RMS amplitude averaged between the 144 and 572
167 Hz channels (black) and selected peaks (red); g) EFI Ex, Ey, Ez electric field components
168 in burst mode; h) FGM Bx, By, Bz , |B| magnetic field; i) ESA ion Vx, Vy, Vz velocity
169 components. The electric and magnetic time series and ion velocities are plotted in GSM
170 coordinates (x: blue, y: green, and z: red curves). The magnetic field magnitude is plotted
171 in black.

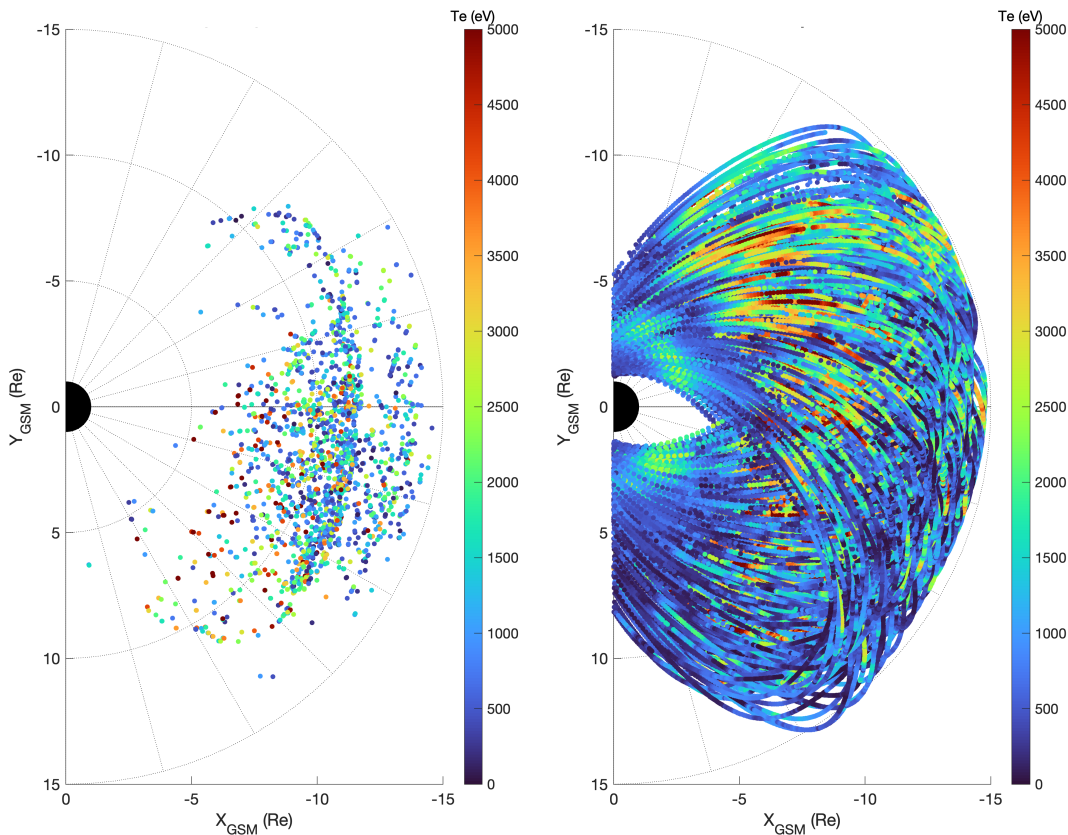
172

173 **4. Automated Event Detection Algorithm and BBF Selection Criteria**

174 In this section, we describe the event search criteria. First, we identify intervals of strong
175 electric fields. For this, we select electric field peaks from the onboard computed electric
176 field RMS amplitude recorded by the filterbank. The advantage of using FBK is that it
177 provides continuous coverage, as opposed to the sporadic burst intervals where high-
178 cadence electric field time series are recorded. Filterbank data contain RMS amplitudes
179 in multiple frequency channels, from 2.2 to 2689 Hz (Cully et al., 2008). The average
180 between the second, 144 Hz and the third, 572 Hz channels is used as these channels
181 were found to be least contaminated by other wave modes, e.g., chorus, hiss and ultra-
182 low-frequency waves. After checking and removing data spikes, we compute a moving
183 average and standard deviation within a 30-minute window and subtract the moving
184 average from the signal. We select all the points exceeding three standard deviations,
185 further referred to as peaks. Overall, we have analyzed 25,698,639 FBK data points and
186 identified 317,416 peaks. The remaining 25,381,223 data points are referred to as non-
187 peaks.

188 Strong electric fields are not specific to bursty bulk flows and can naturally occur
189 in various regions of the magnetosphere, for example, they can be associated with inner
190 magnetospheric plasma wave modes, e.g., time-domain structures (TDS; e.g., Mozer et
191 al., 2013; 2015). In this study, we focus on electron energization in BBFs, hence we set
192 additional criteria to select BBF events: magnetic field fluctuations, $|dB|$ must exceed 5
193 nT and the maximum ion speed within a ± 30 second interval around the identified electric
194 field peak must be greater than 100 km/s. These additional selection criteria were used

195 for the statistical analysis presented below. In addition, we set two different thresholds for
 196 the minimum electric field amplitude, >0.1 mV/m and >1 mV/m to examine the relationship
 197 between electric field amplitude and electron heating. Figure 2 shows the distribution of
 198 6528 peaks with amplitude >0.1 mV/m peaks (left) and 25,381,223 non-peaks (right) on
 199 a scatter plot in the GSM coordinates (the Sun is on the left). The color indicates ESA
 200 electron temperature. Overall, the spatial distribution of events is consistent with Ergun
 201 et al. (2015). Most events are located at $Re=5-15$, consistent with the BBF braking region.
 202 The duskside prevalence is in line with reported occurrences of BBFs (e.g., Raj et
 203 al., 2002). Similar dawn-dusk occurrence rate asymmetry was seen in the magnetotail for
 204 both depolarizing flux bundles and injections (Liu et al., 2013; 2016; Gabrielse et
 205 al., 2014), likely caused by asymmetric tail reconnection (Nagai et al., 2013). The large
 206 number of events just inside of 12 Re is due to the spacecraft dwell time at their apogee.
 207 To eliminate this bias, we binned the data on the XY_{GSM} -grid at 0.5 Re resolution and
 208 plotted the event occurrence distribution normalized by the spacecraft dwell time in Figure
 209 3.

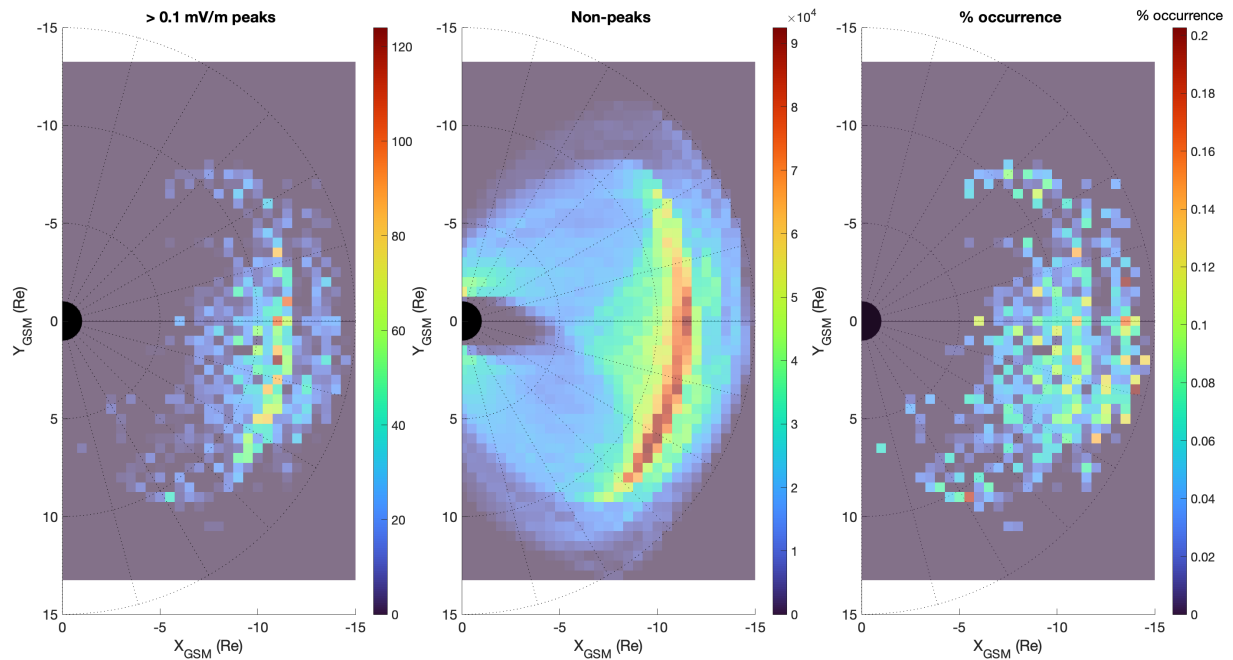


210

211 **Figure 2.** Scatter plot of >0.1 mV/m peaks (left) and non-peaks (right). Color represents
 212 the ESA electron temperature.

213

214 The diagrams in Figure 3 show the number of >0.1 mV/m peaks (left), non-peaks (center),
 215 and peaks' % occurrence (right). The occurrence rate of peaks is uniform and relatively
 216 low, ~0.1% demonstrating the transient nature of these events.



217

218 **Figure 3.** Diagrams showing the number of >0.1 mV/m peaks (left), non-peaks (center),
 219 and peaks' % occurrence (right).

220

221 Figure 4 shows electron temperature for >0.1 mV/m peaks (left) and non-peaks (center).

222 The percent difference between the peaks' and non-peaks' temperature,

223 $\frac{T_{e_{peaks}} - T_{e_{non-peaks}}}{T_{e_{peaks}}} \cdot 100\%$ is shown in the right panel. The temperature distribution is

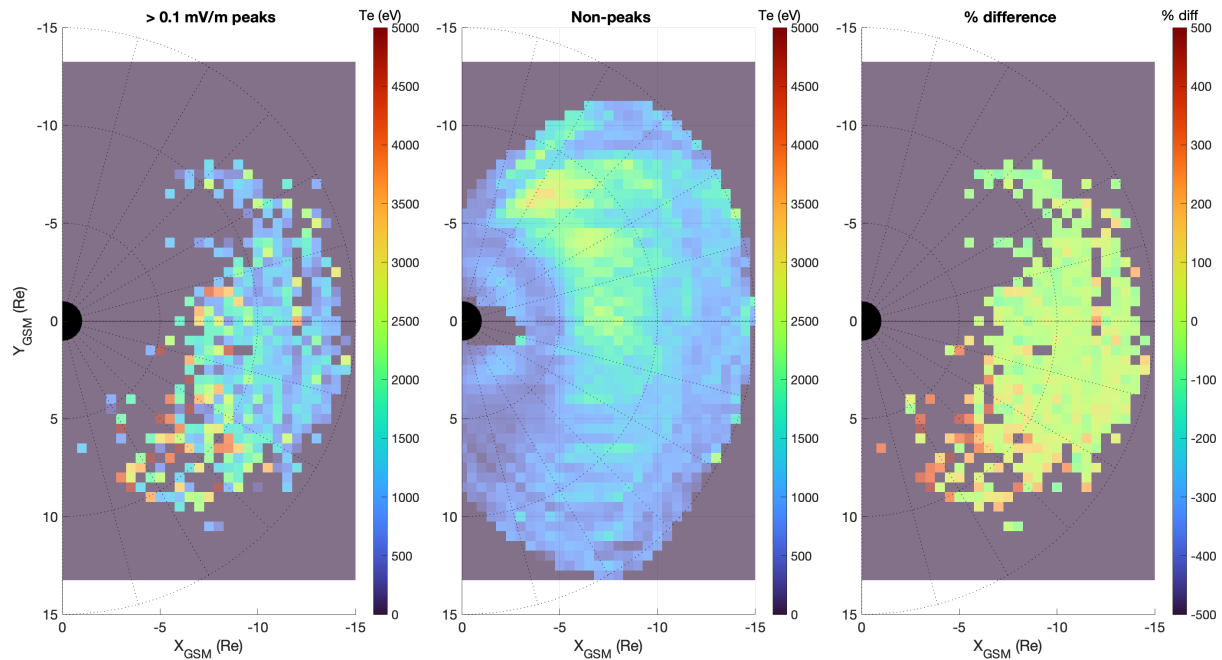
224 different for peaks and non-peaks. For peaks, it maximizes at ~5 keV in the dusk sector,
 225 ~19-21 MLT and radial distances from 5 to 10 Re, and gradually decreases towards dawn.

226 For non-peaks, the trend is opposite: the maximum temperature, ~3 keV is observed near
 227 dawn. The latter dawn-dusk asymmetry is consistent with previous THEMIS observations

228 of electron temperature that attributed the asymmetry to the eastward electron drift and
 229 simultaneous adiabatic energization (e.g., Wang et al., 2012; Dubyagin et al., 2016; Ma

230 et al., 2020). This contrast between the peaks' and non-peaks' trends results in the

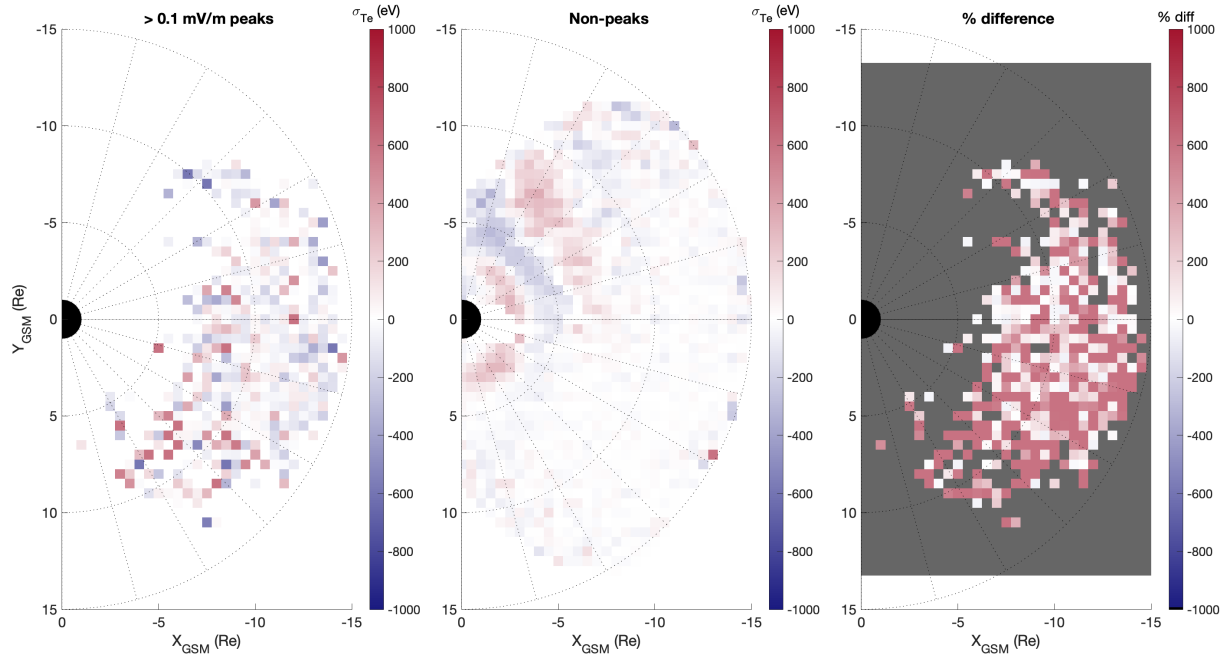
231 percent difference being positive (~300-400%) in the dusk sector and negative (~-100%)
 232 in the dawn sector. A similar distribution is observed for >1 mV/m peaks (not shown here).



233
 234 **Figure 4.** ESA electron temperature for >0.1 mV/m peaks (left) and non-peaks (center).
 235 The percent difference between the peaks' and non-peaks' temperature (right).
 236

237 5. Electric Field Amplitude and Electron Temperature and Energetic Flux Variations

238 Here we discuss a relationship between the electric field amplitude and fluctuations in
 239 electron temperature and energetic electron fluxes. The ESA temperature is
 240 representative of core population while SST measurements depict the behavior of more
 241 energetic electrons at the tail of electron distribution. The left-hand panels of Figures 5
 242 and 6 show electron temperature fluctuations for two electric field RMS thresholds, >0.1
 243 mV/m and >1 mV/m, respectively. The center panels show electron temperature
 244 fluctuations for non-peaks, and the right-hand panels show a percent difference between
 245 the peaks and non-peaks, $\frac{|\sigma_{Te_{peaks}}| - |\sigma_{Te_{non-peaks}}|}{|\sigma_{Te_{peaks}}|} \cdot 100\%$. The temperature fluctuations
 246 reach their maximum, $\sim \pm 1$ keV for peaks; especially in the dusk sector. The fluctuations
 247 also increase for non-peaks in the morning sector, however they are generally less
 248 pronounced. The difference between the peaks and non-peaks is positive, up to $\sim 1000\%$
 249 as shown in the right-hand side panels.

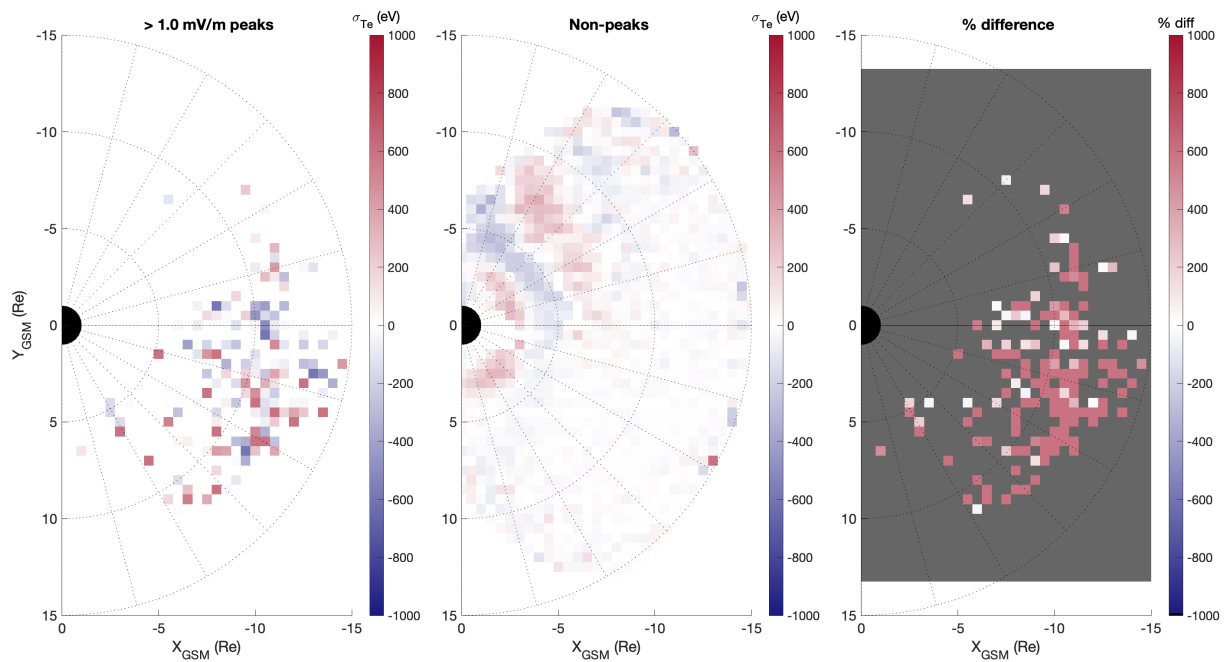


250

251 **Figure 5.** Electron temperature fluctuations for >0.1 mV/m peaks (left), non-peaks
 252 (center) and % difference between the peaks and non-peaks (right).

253

254 The difference becomes even more distinct for high-amplitude, >1 mV/m peaks, where it
 255 often approaches or even exceeds 1000% as demonstrated in Figure 6. This indicates
 256 that the temperature fluctuations increase with electric field amplitude.



257

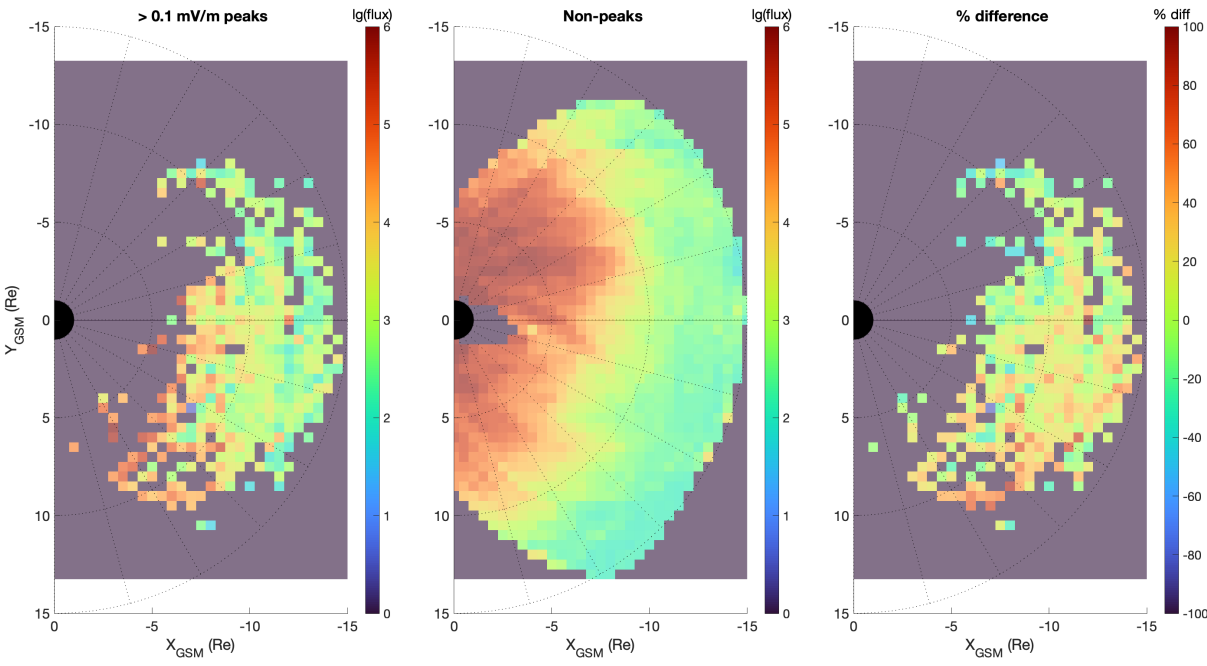
258 **Figure 6.** Electron temperature fluctuations for >1 mV/m peaks (left), non-peaks (center)
 259 and % difference between the peaks and non-peaks (right).

260
 261 Similarly, we analyzed variations in the 139 keV electron fluxes. Figures 7 and 8 show
 262 flux variations plotted on a logarithmic scale for two electric field RMS thresholds, >0.1
 263 mV/m and >1 mV/m, respectively. The center panels show 139 keV electron flux
 264 variations for non-peaks, and the right-hand panels show a percent difference between

265 the peaks and non-peaks, $\frac{\log(|\sigma_{flux_{peaks}}|) - \log(|\sigma_{flux_{non-peaks}}|)}{\log(|\sigma_{flux_{peaks}}|)} \cdot 100\%$.

266 The flux variations increase towards Earth in both cases, peaks and non-peaks. They
 267 maximize in the duskside region for peaks. For non-peaks, enhanced variations are
 268 observed in the radiation belt region. The resultant percent difference between peaks and
 269 non-peaks is largest in the dusk sector adjacent to the outer radiation belt.

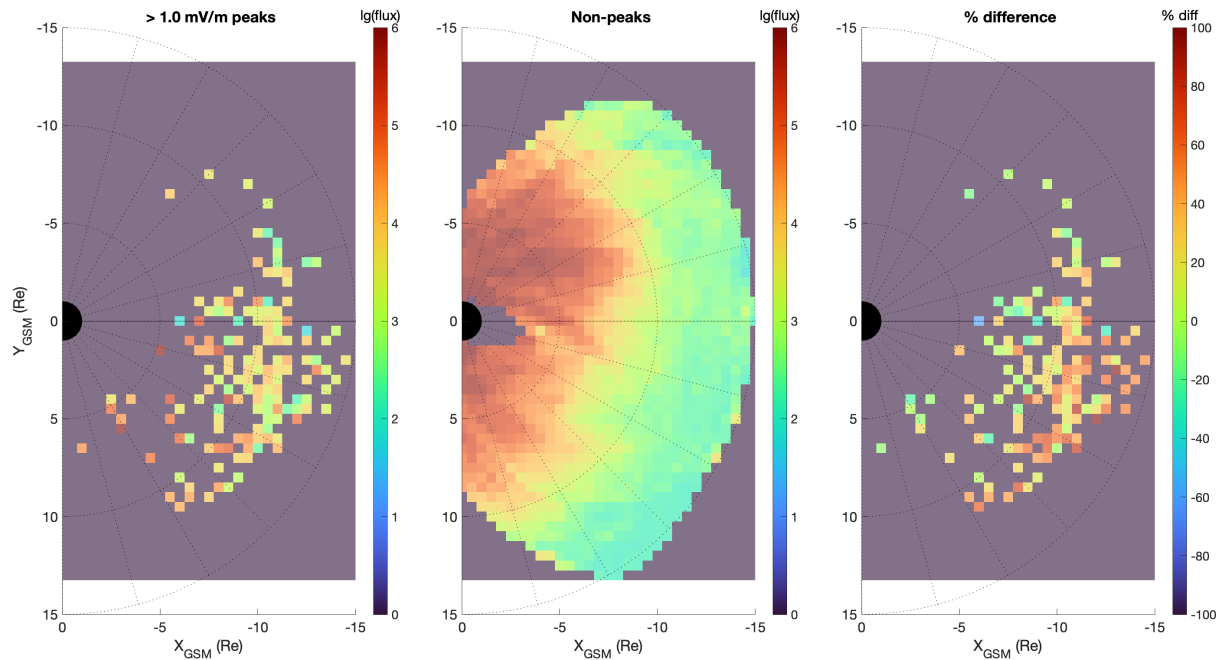
270



271
 272 **Figure 7.** 139 keV electron flux variations for >0.1 mV/m peaks (left), non-peaks (center)
 273 and % difference between the lg(flux) for peaks and non-peaks (right).

274
 275 The higher electric field threshold peaks are associated with more pronounced flux
 276 variations that span a larger region in both the azimuthal and radial directions (as

277 illustrated in Figure 8). The percent difference between peaks and non-peaks is also
278 larger than for >0.1 mV/m electric fields, as observed in the pre-midnight sector.



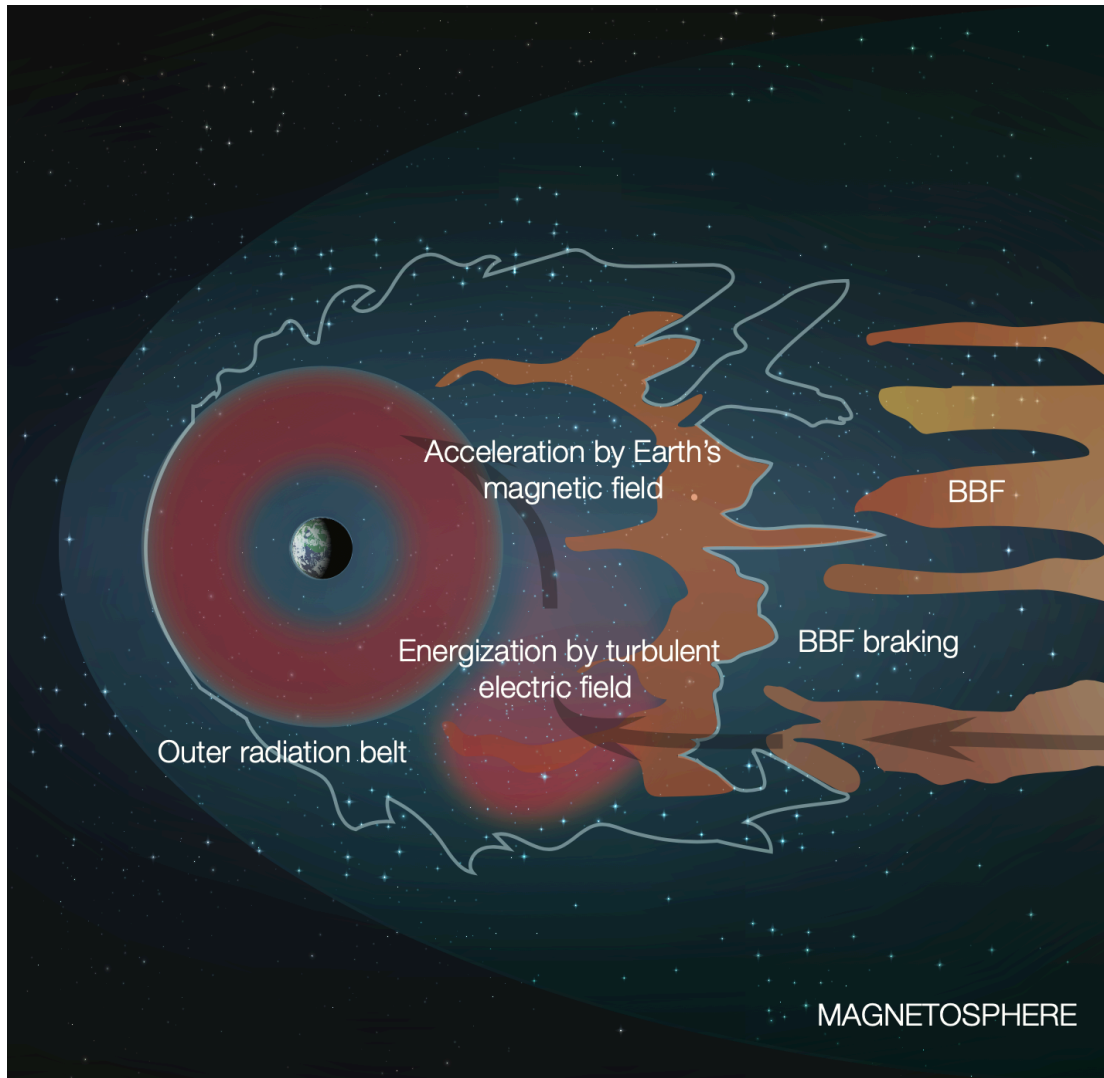
279
280 **Figure 8.** 139 keV electron flux variations for >1 mV/m peaks (left), non-peaks (center)
281 and % difference between the $\log(\text{flux})$ for peaks and non-peaks (right).

282

283 **6. Discussion. The Role of Pre-energized Electron Population in Supplying the** 284 **Outer Radiation Belt**

285 The potential role of pre-energized electron population in supplying the outer radiation
286 belt is summarized in a schematic in Figure 9. The schematic outlines the scenario where
287 energy is initially being transferred from BBFs to electrons via the large turbulent electric
288 fields. The BBFs are drawn following high-resolution magnetohydrodynamic simulations
289 of BBFs by Wiltberger et al. (2015). The region where electron energization in large
290 amplitude electric fields takes place is based on the analysis presented here. The intense,
291 turbulent electric fields develop primarily in the BBF braking region which extends from
292 ~ 12 Re to the outer edge of the radiation belts. If an energized tail (>100 keV) in the
293 electron distribution develops from the turbulent electric fields as the data suggest, it is
294 further accelerated as the electrons continue their eastward and inward drift to regions of
295 higher magnetic field strengths. Essentially, the turbulent electric fields create a seed
296 population that can lead to MeV electrons in the radiation belt. A detailed analysis of

297 electron energization and injection by BBFs using electron trajectory tracing in high-
298 resolution magnetohydrodynamic field output from Lyon-Fedder-Mobarry model is
299 presented by Eshetu et al. (2018). They examined the difference between energization
300 of low and high energy electrons and showed that the process is adiabatic for $\sim < 10$ keV
301 electrons and non-adiabatic for higher energy electrons. In relation to this study, these
302 results have the following implications. The injection inward of ~ 10 Re is a combination
303 of grad-B and ExB drift directed towards Earth. As the electrons move inward, the dipole
304 magnetic field starts to dominate such that electrons drift eastward due to grad-B drift.
305 For lower energy core population (\sim a few keV), the initial temperature enhancement will
306 be amplified proportionally to the background magnetic field. In a situation where 5 keV
307 electrons propagate from ~ 10 nT tail magnetic field to geosynchronous orbit where B is
308 ~ 100 nT, they will get energized by 10 times to 50 keV. The effect will be more
309 pronounced if electron injections propagate down to $L \sim 3$ (though these events are much
310 rarer) where B is ~ 1000 nT resulting in ~ 100 times energization to 500 keV. Electrons,
311 initially energized by turbulent electric fields to ~ 100 keV (as seen in the SST flux) will
312 also be accelerated by about ten times, to \sim MeV if they propagate to the geosynchronous
313 orbit and more if they get farther in, though their motion will no longer be adiabatic, thus
314 not conserving the first adiabatic invariant. Thus, this pre-energized electron population
315 may contribute to a significant fraction of energetic tail of the outer radiat
316



317

318 **Figure 9.** Schematic showing the cascade of energy transfer from BBFs to the outer
 319 radiation belt. Based on high-resolution magnetohydrodynamic simulations of BBFs by
 320 Wiltberger et al. (2015).

321

322 7. Conclusions

323 High amplitude electric fields in the BBF regions are associated with increases of electron
 324 temperature by three times compared to the intervals when they are not observed and
 325 cause ten-fold electron temperature fluctuations. They are also associated with variations
 326 in energetic energy fluxes in a wide range of energy. There is a clear correlation between
 327 the field amplitude and electron temperature and energetic flux variations: stronger fields
 328 are related to larger variations, indicative of a local acceleration process. Though these

329 events are transient and their occurrence is less than 1%, their impact on the
330 magnetospheric dynamics may be rather significant. As the locally pre-energized by an
331 order of magnitude electrons travel toward the inner magnetosphere and get further
332 accelerated by the increasing magnetic field, they supply the high-energy tail of the outer
333 radiation belt.

334

335 **Acknowledgments**

336 This work was supported by NASA grants for THEMIS mission and funding support from
337 the MMS and Van Allen Probes missions. We acknowledge NASA contract NAS5-02099
338 and V. Angelopoulos for use of data from the THEMIS Mission. Specifically, J. W. Bonnell
339 and F. S. Mozer for use of EFI data, D. Larson and the late R. P. Lin for use of SST data,
340 C. W. Carlson and J. P. McFadden for use of ESA data, K. H. Glassmeier, U. Auster and
341 W. Baumjohann for the use of FGM data provided under the lead of the Technical
342 University of Braunschweig and with financial support through the German Ministry for
343 Economy and Technology and the German Center for Aviation and Space (DLR) under
344 contract 50 OC 0302.

345

346 **Data availability**

347 THEMIS data is available at <http://themis.ssl.berkeley.edu/data/themis/>.

348

349 **References**

350

351 El-Alaoui, M., R. L. Richard, M. Ashour-Abdalla, M. L. Goldstein, and R. J.
352 Walker (2013), Dipolarization and turbulence in the plasma sheet during a substorm:
353 THEMIS observations and global MHD simulations, *J. Geophys. Res. Space*
354 *Physics*, 118, 7752–7761, doi:[10.1002/2013JA019322](https://doi.org/10.1002/2013JA019322).

355

356 Angelopoulos, V., W. Baumjohann, C. F. Kennel, F. V. Coroniti, M. G. Kivelson, R.
357 Pellat, R. J. Walker, H. Lohr, and G. Paschmann (1992), Bursty bulk flows in the inner
358 central plasma sheet, *J. Geophys. Res.*, 97(A4), 4027–4039, doi:[10.1029/91JA02701](https://doi.org/10.1029/91JA02701).

359

360 Angelopoulos, V., C. F. Kennel, F. V. Coroniti, R. Pellat, M. G. Kivelson, R. J.
361 Walker, C. T. Russel, W. Baumjohann, W. C. Feldman, and J. T.
362 Gosling (1994), Statistical characteristics of bursty bulk flow events, *J. Geophys.*
363 *Res.*, 99(A11), 21,257–21,280, doi:[10.1029/94JA01263](https://doi.org/10.1029/94JA01263).

364

365 Angelopoulos, V., et al. (1997), Magnetotail flow bursts: Association to global
366 magnetospheric circulation, relationship to ionospheric activity and direct evidence for
367 localization, *Geophys. Res. Lett.*, 24(18), 2271–2274, doi:[10.1029/97GL02355](https://doi.org/10.1029/97GL02355).
368

369 Angelopoulos, V. (2008), The THEMIS mission, *Space Sci. Rev.*, 141, 5–34,
370 doi:[10.1007/s11214-008-9336-1](https://doi.org/10.1007/s11214-008-9336-1).
371

372 Angelopoulos, V., Sibeck, D., Carlson, C.W. et al. (2008), First Results from the THEMIS
373 Mission. *Space Sci Rev.*, 141, 453–476, <https://doi.org/10.1007/s11214-008-9378-4>.
374

375 Auster, H. U., et al. (2008), The THEMIS fluxgate magnetometer, *Space Sci.*
376 *Rev.*, 141, 235–264, doi:[10.1007/s11214-008-9365-9](https://doi.org/10.1007/s11214-008-9365-9).
377

378 Baumjohann, W., G. Paschmann, and H. Lühr (1990), Characteristics of high-speed ion
379 flows in the plasma sheet, *J. Geophys. Res.*, 95(A4), 3801–3809,
380 doi:[10.1029/JA095iA04p03801](https://doi.org/10.1029/JA095iA04p03801).
381

382 Bonnell, J. W., F. S. Mozer, G. T. Delory, A. J. Hull, R. E. Ergun, C. M. Cully, V.
383 Angelopoulos, and P. R. Harvey (2008), The Electric Field Instrument (EFI) for
384 THEMIS, *Space Sci. Rev.*, 141, 303–341, doi:[10.1007/s11214-008-9469-2](https://doi.org/10.1007/s11214-008-9469-2).
385

386 Chaston, C. C., J. W. Bonnell, L. Clausen, and V. Angelopoulos (2012), Energy transport
387 by kinetic-scale electromagnetic waves in fast plasma sheet flows, *J. Geophys.*
388 *Res.*, 117, A09202, doi:[10.1029/2012JA017863](https://doi.org/10.1029/2012JA017863).
389

390 Chaston, C. C., et al. (2014), Observations of kinetic scale field line
391 resonances, *Geophys. Res. Lett.*, 41, 209–215, doi:[10.1002/2013GL058507](https://doi.org/10.1002/2013GL058507).
392

393 Chen, C. X., and R. A. Wolf (1993), Interpretation of high-speed flows in the plasma
394 sheet, *J. Geophys. Res.*, 98(A12), 21,409–21,419, doi:[10.1029/93JA02080](https://doi.org/10.1029/93JA02080).
395

396 Cully, C. M., R. E. Ergun, K. Stevens, A. Nammari, and J. Westfall (2008), The THEMIS
397 digital fields board, *Space Sci. Rev.*, 141, 343–355, doi:[10.1007/s11214-008-9417-1](https://doi.org/10.1007/s11214-008-9417-1).
398

399 Dai, L., J. R. Wygant, C. Cattell, J. Dombeck, S. Thaller, C. Mouikis, A. Balogh, and H.
400 Rème (2011), Cluster observations of surface waves in the ion jets from magnetotail
401 reconnection, *J. Geophys. Res.*, 116, A12227, doi:[10.1029/2011JA017004](https://doi.org/10.1029/2011JA017004).
402

403 Dai, L., Wang, C., Duan, S., He, Z., Wygant, J. R., Cattell, C. A., Tao, X., Su,
404 Z., Kletzing, C., Baker, D. N., et al. (2015), Near-Earth injection of MeV electrons
405 associated with intense dipolarization electric fields: Van Allen Probes
406 observations, *Geophys. Res. Lett.*, 42, 6170– 6179, doi:[10.1002/2015GL064955](https://doi.org/10.1002/2015GL064955).
407

408 Delcourt, D. C. (2002). Particle acceleration by inductive electric fields in the inner
409 magnetosphere. *Journal of Atmospheric and Solar - Terrestrial Physics*, 64(5-6), 551–
410 559. [10.1016/S1364-6826\(02\)00012-3](https://doi.org/10.1016/S1364-6826(02)00012-3).

411
412 Dubyagin, S., Ganushkina, N. Y., Sillanpää, I., and Runov, A. (2016), Solar wind-
413 driven variations of electron plasma sheet densities and temperatures beyond
414 geostationary orbit during storm times, *J. Geophys. Res. Space*
415 *Physics*, 121, 8343– 8360, doi:[10.1002/2016JA022947](https://doi.org/10.1002/2016JA022947).
416
417 Ergun, R. E., L. Andersson, Y.-J. Su, D. L. Newman, M. V. Goldman, W. Lotko, C. C.
418 Chaston, and C. W. Carlson (2005), Localized parallel electric fields associated with
419 inertial Alfvén waves, *Phys. Plasmas*, 12, 072901.
420
421 Ergun, R. E., et al. (2009), Observations of double layers in Earth's plasma sheet, *Phys.*
422 *Rev. Lett.*, 102, 155002, doi:[10.1103/PhysRevLett.102.155002](https://doi.org/10.1103/PhysRevLett.102.155002).
423
424 Ergun, R. E., Goodrich, K. A., Stawarz, J. E., Andersson, L., and Angelopoulos,
425 V. (2015), Large-amplitude electric fields associated with bursty bulk flow braking in the
426 Earth's plasma sheet. *J. Geophys. Res. Space Physics*, 120, 1832– 1844.
427 doi: [10.1002/2014JA020165](https://doi.org/10.1002/2014JA020165).
428
429 Ergun, R. E. *et al.* (2020), Particle Acceleration in Strong Turbulence in the Earth's
430 Magnetotail,
431 *ApJ*, 898, 153, <https://doi.org/10.3847/1538-4357/ab9ab5>.
432
433 Eshetu, W. W., Lyon, J. G., Hudson, M. K., & Wiltberger, M. J. (2019). Simulations of
434 electron energization and injection by BBFs using high-resolution LFM MHD
435 fields. *Journal of Geophysical Research: Space*
436 *Physics*, 124, 1222– 1238. <https://doi.org/10.1029/2018JA025789>.
437
438 Gabrielse, C., Angelopoulos, V., Runov, A., and Turner, D. L. (2012), The effects of
439 transient, localized electric fields on equatorial electron acceleration and transport toward
440 the inner magnetosphere, *J. Geophys. Res.*, 117, A10213, doi:[10.1029/2012JA017873](https://doi.org/10.1029/2012JA017873).
441
442 Gabrielse, C., Angelopoulos, V., Runov, A., and Turner, D. L. (2014), Statistical
443 characteristics of particle injections throughout the equatorial magnetotail, *J. Geophys.*
444 *Res. Space Physics*, 119, 2512– 2535, doi:[10.1002/2013JA019638](https://doi.org/10.1002/2013JA019638).
445
446 Karimabadi, H., et al. (2013), Coherent structures, intermittent turbulence, and dissipation
447 in high-temperature plasmas, *Phys. Plasmas*, 20, 012,303–012,315,
448 doi:[10.1063/1.4773205](https://doi.org/10.1063/1.4773205).
449
450 Kindel, J. M., and C. F. Kennel (1971), Topside current instabilities, *J. Geophys.*
451 *Res.*, 76(13), 3055–3078, doi:[10.1029/JA076i013p03055](https://doi.org/10.1029/JA076i013p03055).
452
453 Liu, J., V. Angelopoulos, A. Runov, and X.-Z. Zhou (2013), On the current sheets
454 surrounding dipolarizing flux bundles in the magnetotail: The case for wedgelets, *J.*
455 *Geophys. Res. Space Physics*, 118, 2000–2020, doi:[10.1002/jgra.50092](https://doi.org/10.1002/jgra.50092).
456

457 Liu, J., Angelopoulos, V., Zhang, X.-J., Turner, D. L., Gabrielse, C., Runov, A., Li,
458 J., Funsten, H. O., and Spence, H. E. (2016), Dipolarizing flux bundles in the cis-
459 geosynchronous magnetosphere: Relationship between electric fields and energetic
460 particle injections, *J. Geophys. Res. Space Physics*, 121, 1362–1376,
461 doi:[10.1002/2015JA021691](https://doi.org/10.1002/2015JA021691).
462

463 Lysak, R. L., Y. Song, and T. W. Jones (2009), Propagation of Alfvén waves in the
464 magnetotail during substorms, *Ann. Geophys.*, 27, 2237–2246, doi:[10.5194/angeo-27-
465 2237-2009](https://doi.org/10.5194/angeo-27-2237-2009).
466

467 Ma, X., Nykyri, K., Dimmock, A., & Chu, C. (2020). Statistical study of solar wind,
468 magnetosheath, and magnetotail plasma and field properties: 12+ years of THEMIS
469 observations and MHD simulations. *Journal of Geophysical Research: Space
470 Physics*, 125, e2020JA028209. <https://doi.org/10.1029/2020JA028209>.
471

472 McFadden, J. P., C. W. Carlson, D. Larson, M. Ludlan, R. Abiad, B. Elliott, P. Turin, M.
473 Marckwordt, and V. Angelopoulos (2008), The THEMIS ESA plasma instrument and in-
474 flight calibration, *Space Sci. Rev.*, 141, 277–302, doi:[10.1007/s11214-008-9440-2](https://doi.org/10.1007/s11214-008-9440-2).
475

476 Motoba, T., Ohtani, S., Claudepierre, S.G., Reeves, G.D., Ukhorskiy, A.Y. and Lanzerotti,
477 L.J. (2020), Dynamic Properties of Particle Injections Inside Geosynchronous Orbit: A
478 Multisatellite Case Study. *J. Geophys. Res. Space Physics*, 125:
479 e2020JA028215. <https://doi.org/10.1029/2020JA028215>.
480

481 Mozer, F. S., S. D. Bale, J. W. Bonnell, C. C. Chaston, I. Roth, and J. Wygant
482 (2013), Megavolt parallel potentials arising from double-layer streams in the Earth's outer
483 radiation belt, *Phys. Rev. Lett.*, 111(23), 235002, doi:[10.1103/PhysRevLett.111.235002](https://doi.org/10.1103/PhysRevLett.111.235002).
484

485 Mozer, F. S., Agapitov, O. V., Artemyev, A., Drake, J. F., Krasnoselskikh, V., Lejosne,
486 S., and Vasko, I. (2015), Time domain structures: What and where they are, what they
487 do, and how they are made. *Geophys. Res. Lett.*, 42, 3627–3638.
488 doi: [10.1002/2015GL063946](https://doi.org/10.1002/2015GL063946).
489

490 Nagai, T., I. Shinohara, S. Zenitani, R. Nakamura, T. K. M. Nakamura, M. Fujimoto, Y.
491 Saito, and T. Mukai (2013), Three-dimensional structure of magnetic reconnection in the
492 magnetotail from Geotail observations, *J. Geophys. Res. Space Physics*, 118, 1667–
493 1678, doi:[10.1002/jgra.50247](https://doi.org/10.1002/jgra.50247).
494

495 Nakamura, R., et al. (2014), Low-altitude electron acceleration due to multiple flow bursts
496 in the magnetotail, *Geophys. Res. Lett.*, 41, 777–784, doi:[10.1002/2013GL058982](https://doi.org/10.1002/2013GL058982).
497

498 Newman, D. L., M. V. Goldman, R. E. Ergun, and A. Mangeney (2001), Formation of
499 double layers and electron holes in a current-driven space plasma, *Phys. Rev.
500 Lett.*, 87(25), 255001, doi:[10.1103/PhysRevLett.87.255001](https://doi.org/10.1103/PhysRevLett.87.255001).
501

502 Nishimura, Y., J. Wygant, T. Ono, M. Iizima, A. Kumamoto, D. Brautigam, and F.
503 Rich (2008), Large-amplitude wave electric field in the inner magnetosphere during
504 substorms, *J. Geophys. Res.*, 113, A07202, doi:[10.1029/2007JA012833](https://doi.org/10.1029/2007JA012833).
505

506 Ohtani, S., Shay, M. A., and Mukai, T. (2004), Temporal structure of the fast convective
507 flow in the plasma sheet: Comparison between observations and two-fluid simulations, *J.*
508 *Geophys. Res.*, 109, A03210, doi:[10.1029/2003JA010002](https://doi.org/10.1029/2003JA010002).
509

510 Raj, A., T. Phan, R. P. Lin, and V. Angelopoulos (2002), Wind survey of high-speed bulk
511 flows and field-aligned beams in the near-Earth plasma sheet, *J. Geophys.*
512 *Res.*, 107(A12), 1419, doi:[10.1029/2001JA007547](https://doi.org/10.1029/2001JA007547).
513

514 Sigsbee, K., Cattell, C. A., Fairfield, D., Tsuruda, K., and Kokubun, S., (2002), Geotail
515 observations of low-frequency waves and high-speed earthward flows during substorm
516 onsets in the near magnetotail from 10 to 13 R_E , *J. Geophys. Res.*, 107(A7),
517 doi:[10.1029/2001JA000166](https://doi.org/10.1029/2001JA000166).
518

519 Shiokawa, K., W. Baumjohann, and G. Haerendel (1997), Braking of high-speed flows in
520 the near-Earth tail, *Geophys. Res. Lett.*, 24(10), 1179–1182, doi:[10.1029/97GL01062](https://doi.org/10.1029/97GL01062).
521

522 Sorathia, K. A., Ukhorskiy, A. Y., Merkin, V. G., Fennell, J. F., & Claudepierre, S.
523 G. (2018). Modeling the depletion and recovery of the outer radiation belt during a
524 geomagnetic storm: Combined MHD and test particle simulations. *Journal of Geophysical*
525 *Research: Space Physics*, 123, 5590– 5609. <https://doi.org/10.1029/2018JA025506>.
526

527 Stawarz, J. E., Ergun, R. E., and Goodrich, K. A. (2015), Generation of high-frequency
528 electric field activity by turbulence in the Earth's magnetotail. *J. Geophys. Res. Space*
529 *Physics*, 120, 1845– 1866. doi: [10.1002/2014JA020166](https://doi.org/10.1002/2014JA020166).
530

531 Ukhorskiy, A. Y., Sitnov, M. I., Merkin, V. G., Gkioulidou, M., and Mitchell, D.
532 G. (2017), Ion acceleration at dipolarization fronts in the inner magnetosphere, *J.*
533 *Geophys. Res. Space Physics*, 122, 3040– 3054, doi:[10.1002/2016JA023304](https://doi.org/10.1002/2016JA023304).
534

535 Ukhorskiy, A. Y., Sorathia, K. A., Merkin, V. G., Sitnov, M. I., Mitchell, D. G.,
536 & Gkioulidou, M. (2018). Ion trapping and acceleration at dipolarization fronts: High-
537 resolution MHD and test-particle simulations. *Journal of Geophysical Research: Space*
538 *Physics*, 123, 5580– 5589. <https://doi.org/10.1029/2018JA025370>.
539

540 Wang, C.-P., Gkioulidou, M., Lyons, L. R., and Angelopoulos, V. (2012), Spatial
541 distributions of the ion to electron temperature ratio in the magnetosheath and plasma
542 sheet, *J. Geophys. Res.*, 117, A08215, doi:[10.1029/2012JA017658](https://doi.org/10.1029/2012JA017658).
543

544 Williams, D. J., D. G. Mitchell, C. Y. Huang, L. A. Frank, and C. T. Russell (1990), Particle
545 acceleration during substorm growth and onset, *Geophys. Res. Lett.*, 17(5), 587–590,
546 doi:[10.1029/GL017i005p00587](https://doi.org/10.1029/GL017i005p00587).
547

548 Wiltberger, M., Merkin, V., Lyon, J. G., and Ohtani, S. (2015), High-resolution global
549 magnetohydrodynamic simulation of bursty bulk flows. *J. Geophys. Res. Space*
550 *Physics*, 120, 4555–4566. doi: [10.1002/2015JA021080](https://doi.org/10.1002/2015JA021080).
551
552 Wygant, J. R., et al. (2002), Evidence for kinetic Alfvén waves and parallel electron
553 energization at 4–6 R_E altitudes in the plasma sheet boundary layer, *J. Geophys.*
554 *Res.*, 107(A8), 1201, doi:[10.1029/2001JA900113](https://doi.org/10.1029/2001JA900113).